Modeling of the heating phenomena in ultrasonic welding of thermoplastic composites with flat energy directors

Arthur Lévy, Steven Le Corre, Irene Fernandez Villegas

Title: Modeling of the heating phenomena in ultrasonic welding ofthermoplastic composites with flat energy directors

Author: Arthur Levy Steven Le Corre Irene Fernandez Villegas

PII: S0924-0136(14)00050-8
DOI: http://dx.doi.org/doi:10.1016/j.jmatprotec.2014.02.009
Reference: PROTEC 13896

To appear in: *Journal of Materials Processing Technology*

Received date: 17-9-2013
Revised date: 31-1-2014
Accepted date: 4-2-2014

Please cite this article as: Arthur Levy, Steven Le Corre, Irene Fernandez Villegas, Modeling of the heating phenomena in ultrasonic welding ofthermoplastic composites with flat energy directors, *Journal of Materials Processing Tech.* (2014), http://dx.doi.org/10.1016/j.jmatprotec.2014.02.009

Highlights

• A multiphysical model of the ultrasonic welding process was developed.

• Dry friction at the interface and bulk viscoelastic heating were taken into account.

• Extensive material characterization was performed for thermoplastic PEI to input in the model.

• The predicted dissipated power compares well with experimental measurements.

• The model provides a realistic prediction of the temperatures in the welding area, which is difficult to measure accurately.

Modeling of the heating phenomena in ultrasonic welding of thermoplastic composites with flat energy directors

Arthur Levy[a], Steven Le Corre[b,*], Irene Fernandez Villegas[c]

[a]Department of Mechanical Engineering, McGill University, 817 Sherbrooke St. West, Montréal QC, H3A 0C3, Canada.
[b]Laboratoire de Thermocinétique de Nantes, La Chantrerie, rue Christian Pauc, BP 50609, 44306 Nantes cedex 3, France.
[c]Structural Integrity and Composites, Delft University of Technology, Kluyverweg 1, 2629 HS Delft, The Netherlands.

Abstract

A model for the mechanics (oscillating deformation), heat transfer including viscoelastic heat generation and friction dissipation, and degree of adhesion (intimate contact and healing) is proposed for the initial transient heating phase.

Numerical resolution was performed using a multi-physical finite element code. The predicted dissipated power evolution exhibits a good correlation with previous experimental measurement of delivered power, and shows that the apparatus has a global efficiency of 13%. The predicted degree of adhesion also confirms the experimental observation that adhesion starts at the edge of the contact area, and progressively extends to the whole contact area.

The numerical model was further used to investigate the physical mechanisms occurring during the welding process. As suggested in the literature, the first heating mechanism is confirmed to be due to interfacial friction. Bulk viscoelastic dissipation becomes predominant when the interface reaches higher temperatures. The dissipated power is suddenly increased when the whole interface reaches the glass transition temperature.

Keywords: thermoplastic composite, energy directors, ultrasonic welding, viscoelastic heating, friction heating, multiphysical simulation

1. Introduction

Thermoplastic composites offer new possibilities for the aerospace industry. Huge structures (several meters) can be processed rapidly and more cost-effectively than when thermoset composites are used, since the latter need to undergo lengthy curing reactions. The ability to fuse thermoplastic resins gives new perspectives for processing and assembling as mentioned by Grewell and Benatar (2007). Fusion bonding,

*Corresponding author, +33 240683113
Email addresses: arthur.levy@mcgill.ca (Arthur Levy), steven.lecorre@univ-nantes.fr (Steven Le Corre), I.FernandezVillegas@tudelft.nl (Irene Fernandez Villegas)

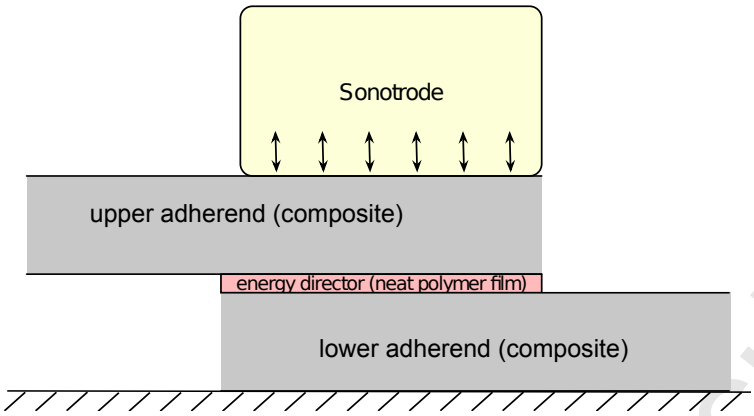

Figure 1: Principle of the ultrasonic welding.

usually known as welding is, indeed, a group of joining techniques specific to thermoplastic composites, that offers a very interesting alternative to traditional assembling via adhesive bonding or mechanical fastening (Yousefpour et al., 2004).

Within this group, ultrasonic welding of thermoplastic composites is based on low-amplitude and high-frequency vibrations that cause surface friction and viscoelastic heating at the welding interface. Its main advantages are very high speed (welding times of a few seconds) and the fact that no foreign material, such as a metal mesh or metal particles, is needed at the interface, regardless the nature of the adherends. As first introduced by Fernandez Villegas (2013), localized heating in ultrasonic welding of thermoplastic composites can be achieved by placing a film of neat matrix at the welding interface (Fig. 1). This straightforward "flat energy director", as defined in this previous work (Fernandez Villegas, 2013), is a solution that contrasts with more traditional and complex energy directors derived from the plastics industry, consisting of neat resin protrusions molded on the surfaces to be welded (Benatar et al., 1989). Flat energy directors concentrate heat dissipation at the welding interface as a result of their lower stiffness and hence their higher cyclic strain, as compared to the fibrous adherends. Since they cover the whole overlap, they provide 100% welded areas without the need for any shape or size optimization as suggested in previous work (Levy et al., 2012).

The experimental study by Fernandez Villegas (2013) coupled with the work of Zhang et al. (2009) on heating of rectangular energy directors gave a relevant insight into the different heating mechanisms and their roles in this ultrasonic process. They particularly highlighted the significant effect of dry friction on the initiation of heating, which is combined to the usual self-heating as described by former author on ultrasonic welding such as Tolunay et al. (1983) or Benatar et al. (1989). Nevertheless, further modeling work is needed in order to fully understand and quantify the phenomena taking place in the flat-energy-director ultrasonic welding process. Of particular importance is the temperature developed at the welding interface and the extension of the heat affected zone (HAZ) in the adherends (Fernandez Villegas, 2013), which are difficult to measure by using thermography or traditional thermocouples. Indeed, on the one hand, the

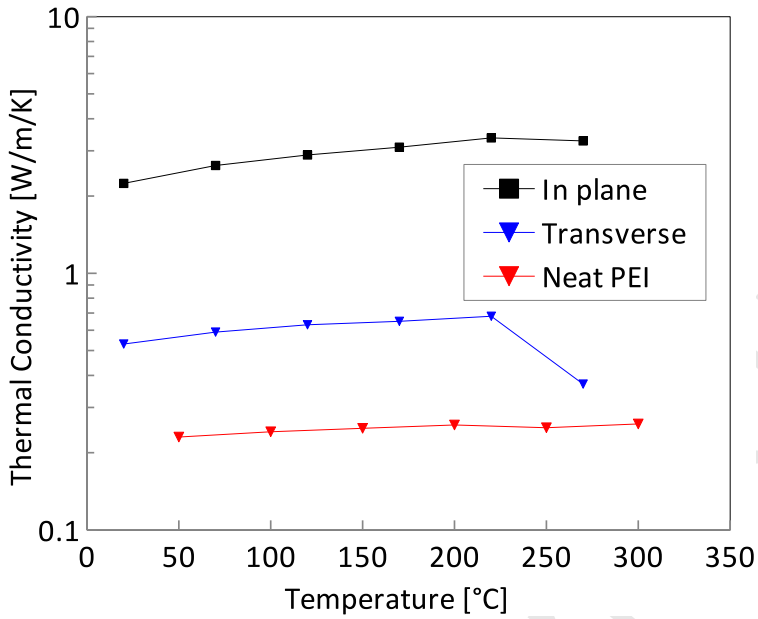

Figure 2: Thermal conductivity of the CF/PEI composite and the neat PEI matrix versus temperature.

HAZ is confined in the vicinity of the overlapping interface, thus not directly visible, and the other hand, introducing a thermocouple at the interface would be very intrusive and might even act as an energy director itself. In order to invetigate the heating mechanisms in the process and to predict the temperature at the welding interface and the extension of the HAZ, a multiphysical model was built and solved in COMSOL Multiphysics.

2. Experimental methods

2.1. Material

The material used for this research was T300 carbon-fiber-fabric (5HS) reinforced polyetherimide (CF/PEI) provided by Ten Cate Advanced Composites, The Netherlands. The modeling of such a welding process requires many thermo-physical parameters that are detailed below. First of all, it is important to note that thermal degradation can be a key problem in thermoplastic welding. It would limit the validity of the present approach. Nevertheless, according to Augh et al. (2001), the values for degradation temperature for CF/PEI, obtained by thermogravimetric analysis, range from 450°C (isothermal mode) to 500°C (non-isothermal mode). As it will be shown later, the temperatures reached in the present process, predicted by the model, are far from this bounds.

The transverse k_{zz} and in-plane k_{xx} thermal conductivity of the composite and of the neat PEI matrix k were measured by DSM R&D Solutions, the Netherlands, using nanoflash tests. They are plotted versus temperature in Fig. 2. In spite of the visible thermo-dependence of the conductivity, the following constant

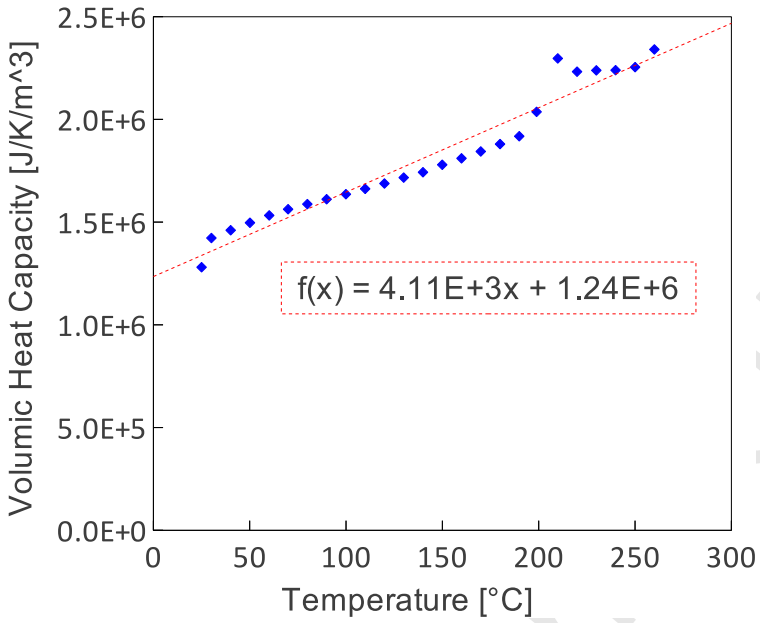

Figure 3: Volumetric heat capacity of the neat PEI matrix $\rho_{PEI}c_p^{PEI}$ versus temperature. It is approximated by a linear relation.

approximations were adopted:

$$\begin{aligned} k_{zz} &= 0.61\,\mathrm{W/mK} \\ k_{xx} &= 2.8\,\mathrm{W/mK} \\ k &= 0.25\,\mathrm{W/mK} \end{aligned} \tag{1}$$

The specific heat capacity c_{PEI} of the neat PEI matrix was measured at TU Delft, using a differential scanning calorimeter (DSC). Its density ρ_{PEI} was measured by the manufacturer Sabic Innovative Plastics using a PVT apparatus. As shown in Fig. 3 the volumetric heat capacity of the PEI $\rho_{PEI}c_{PEI}$ was approximated by the linear relation:

$$\rho_{PEI}c_{PEI} = 4110 \times T\,[^\circ C] + 1.24 \times 10^6\,\mathrm{J/m^3.K}. \tag{2}$$

The viscoelastic mechanical behavior of PEI was studied in Appendix A.

The specific heat capacity c_{comp} of the CF/PEI composite was measured with a DSC. Considering a constant density $\rho_{CF} = 1760\,\mathrm{kg/m^3}$ for the T300 carbon fiber and ρ_{PEI} above, the law of mixtures gives the density of the composite ρ_{comp}. The volumetric heat capacity is plotted versus temperature in Fig. 4. It is in good agreement with the volumetric heat capacity obtained using a law of mixtures:

$$\rho_{comp}c_{comp} = v_f\,(\rho_{CF}c_{CF}) + (1 - v_f)\,(\rho_{PEI}c_{PEI}) \tag{3}$$

where $v_f = 50\%$ is the fiber volume fraction, and $c_{CF} = 800\,\mathrm{J/kg.K}$ the T300 carbon fiber specific heat. Finally, the following linear dependence on temperature was assumed:

$$\rho_{comp}c_{comp} = 2700 \times T\,[^\circ C] + 1.3 \times 10^6\,\mathrm{J/m^3.K}. \tag{4}$$

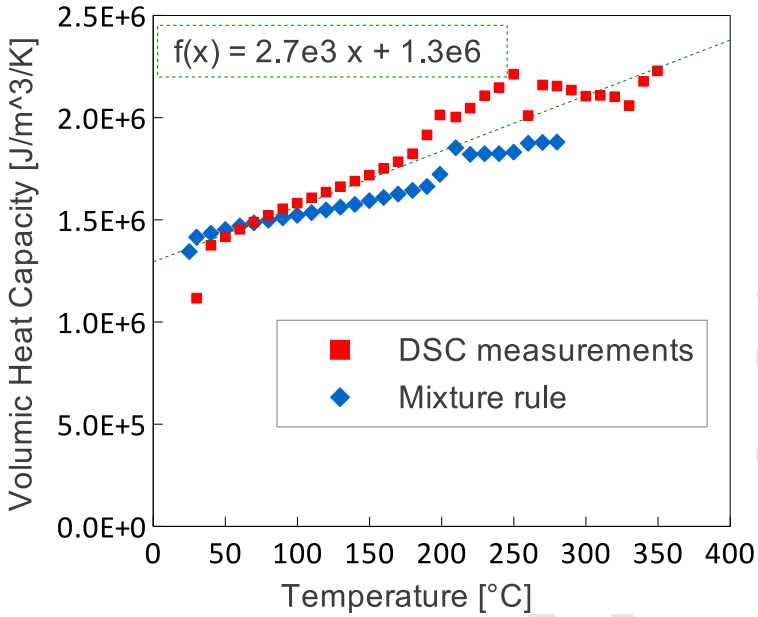

Figure 4: Heat capacity of the CF/PEI composite c_p^{comp} versus temperature. It is approximated by a linear relation.

The in-plane elastic modulus in the warp and weft directions was found by the manufacturer to vary very little (less than 3%) (Tencate Advanced Composites, 2008). Moreover it is rather constant (within 5%) between 23 °C and 80 °C. Nonetheless, the composite adherends are loaded transversely in compression. Therefore, as a first simplified model, the composite is considered isotropic with a Young modulus equal to its transverse modulus. This transverse modulus E_{comp} is evaluated using the rule of mixture proposed by Jacquet et al. (2000) which yields:

$$E_{comp} = 10.3\,\text{GPa}. \tag{5}$$

for a fiber modulus of 180 GPa and a resin modulus of ~ 4 GPa (see Appendix A). A Poisson ratio of 0.4 was used.

2.2. Processing conditions

Six layers of five-harness satin CF reinforced prepreg were used to manufacture the base laminates in a hot platen press. The stacking sequence of the laminates was $[0/90]_{3s}$ and the manufacturing conditions were 20 minutes at 320 °C and 20 bar. The nominal thickness of the consolidated laminates was $h_{plates} = 1.92$ mm.

Rectangular samples (101.6 mm × 25.4 mm) were cut out of the CF/PEI laminates with an abrasive saw, so that the longer side of the samples coincided with the main apparent orientation of the fibers. These samples were degreased and welded in near-field (Benatar et al., 1989), into a single-lap configuration, as illustrated in Fig. 1, with an overlap area of 12.7 mm × 25.4 mm, as indicated by the ASTM D 1002 standard (ASTM International, 2010). A PEI film of thickness $h_{film} = 0.25$ mm was used as a flat energy director.

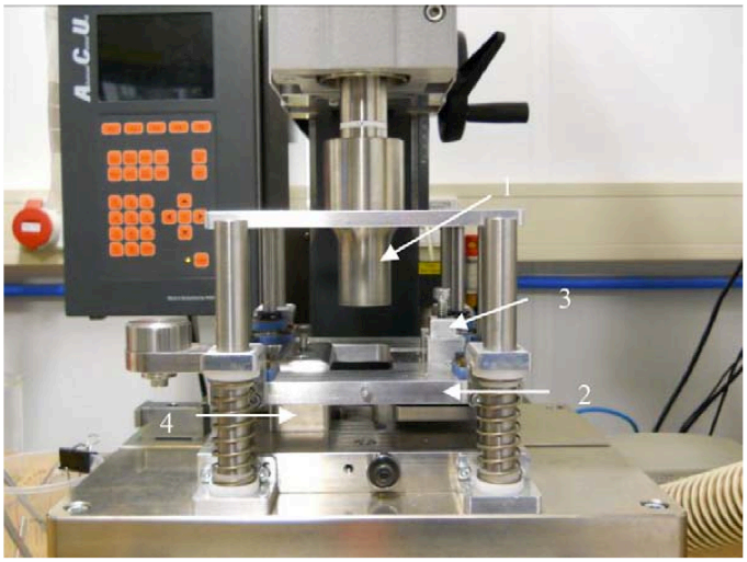

Figure 5: Ultrasonic welding device. 1: sonotrode, 2: sliding platform, 3: clamp for upper sample, 4: clamp for lower sample (Fernandez Villegas, 2013).

For the welding of the samples a 20 kHz Rinco Dynamic 3000 ultrasonic welder with a maximum power input of 3000 W was used. This welding unit automatically adjusts the electrical power input in order to keep the amplitude of vibration constant. It allows for a certain range of amplitude values between 51.8 and 86.2 μm. The edge of the sonotrode in contact with the parts to be welded was cylindrical with a 0.40 mm diameter, much larger than the welding zone. The clamping device, shown in Fig. 5, was designed to allow for vertical motion of the upper adherend and to ensure parallelism between both composite samples. More detail on the apparatus and experimental conditions can be found in Fernandez Villegas (2013).

The processing parameters relevant to the analysis in this paper were:

- welding forces of 300, 1500, and 500 N, which are the minimum, maximum, and an intermediate values of the welder force capability
- vibration amplitudes of 51.8 and 86.2 μm which are the minimum and maximum capabilities of the welder.

It should be noticed that the ultrasonic welder provided feedback on the power dissipated during the process and the displacement of the sonotrode. The dissipated power, as well as the transformations undergone by the flat energy director in the different phases of the process as described in Fernandez Villegas (2013), were used for the validation of the model.

3. Modeling

In this section, a modeling of heating phenomena that enable ultrasonic welding is proposed. Many authors studied the classical case where triangular shape energy directors are used (Nonhof and Luiten, 1996). Tolunay et al. (1983) suggested that the heating is solely due to dissipation of mechanical work through visco-elastic deformation. This suggested phenomenon has been widely assumed in the literature (Benatar and Gutowski, 1989) and allowed to perform analysis of industrial energy director shapes (Wang et al., 2006) or study the effect of design on the process (Suresh et al., 2007). More recently, Levy et al. (2011b) confirmed the heating term due to visco-elastic work dissipation, using time homogenization technique based on asymptotic expansion. An integrated finite element code solving for the vibration, the heat transfer and the flow was developed (Levy et al., 2011a).

In the present study, because the energy director is not triangular but a film at the interface, different phenomena occur. The heating mechanism, as suggested by Zhang et al. (2009) and Fernandez Villegas (2013) also consists in frictional dissipation at the interface which has to be incorporated as an additional interfacial heat source.

3.1. General macroscopic framework

Because of the sample geometry, a plane strain is assumed and the three domains shown in Fig. 1 are described in a two-dimensional framework.

The present study, focuses on the heating phase during ultrasonic welding with flat energy directors. The frameworks is that of Levy et al. (2011a) except that we do not account for the flow, that mostly occur in the subsequent phases of the process Fernandez Villegas (2013).

The physics solved are therefore:

- An elastic problem that describes the vibration effect. The boundary condition being a sinusoidal displacement imposed by the tool. As noticed by Levy et al. (2012), this approach neglects the hammering effect brought up by Tolunay et al. (1983), and considers contact between the sonotrode and the top composite during the whole process. In this study, the contact between the sonotrode and the composite assembly is considered to be lost during a part of the cycle.

- A heat transfer problem that describes temperature evolution in the setup. Following existing work by (Tolunay et al., 1983), the viscoelastic dissipation appears as a thermal source of the form:

$$\dot{Q}_{bulk}(x,y) = \frac{\alpha_h^2 \omega E'' \boldsymbol{\varepsilon}^* : \boldsymbol{\varepsilon}^*}{2} \tag{6}$$

  E'' being the loss modulus of the material and $\boldsymbol{\varepsilon}^*(x,y)$ the amplitude strain tensor obtained by solving one nominal static elastic problem with the amplitude of vibration as a load. Benatar and Gutowski (1989) used a similar approach for their carbon PEEK composite welding study. Levy et al. (2011b)

recovered this term using a time homogenization technique and used it to simulate industrial cases (Levy et al., 2012). Nonhof and Luiten (1996) also retained this heat source but suggested that because of the hammering effect, during an ultrasonic cycle, contact is lost between the sonotrode and the sample. This phenomenon is accounted here by introducing the empirical hammering correction factor α_h in equation (6). If no hammering occurs, $\alpha_h = 1$, and the classical dissipation term from the literature is recovered. In the case of hammering, the sinusoidal strain $\boldsymbol{\varepsilon} = \boldsymbol{\varepsilon}^* \sin(\omega t)$ occurs only during a fraction of the cycle, leading to a reduced viscoelastic dissipation. The data obtained with the nominal problem will be denoted with a star. Using the complex viscosity $\bar{\eta} = \eta' + i\eta'' = \bar{E}/i\omega$ instead ($\bar{E}$ being the complex viscoelastic modulus), equation (6) becomes

$$\dot{Q}_{bulk}(x, y) = \frac{\alpha_h^2 \omega^2 \eta' \boldsymbol{\varepsilon}^* : \boldsymbol{\varepsilon}^*}{2}. \tag{7}$$

It explicitly shows the quadratic dependency of the viscous dissipated power on the vibration frequency.

3.2. Microscopic analysis at the interface

In the following we call "interfaces" the lower and upper interface between the flat energy director and the lower, successively upper, composite adherend.

First the friction phenomenon, that induces an interfacial heat source, cannot be neglected. Then the contact evolution at the microscopic scale is modeled using an intimate contact model.

3.2.1. Friction

Mechanics. Because the stiffness of the neat matrix flat energy director at the interface is lower than that of the composite plates, its longitudinal deformation will be larger than that of the composite resulting in slippage and friction at the interfaces. In order to simulate this displacement discontinuity at the interface, a special connection was considered at the interfaces between the plates and the film. A "thin elastic film", as defined in COMSOL, was assumed with the following anisotropic properties:

- A very high normal stiffness $K_n = 10^{18}\,\mathrm{N/m^3}$ constrains the normal displacement to be continuous, thus ensuring a contact condition.
- A very low initial tangential stiffness $K_t^0 \sim 0$ simulates a perfect slip with no friction. This first model neglects the effect of friction on the deformation and therefore probably over-estimates the slippage. This simple "perfect slip" approach allows one to keep a linear elastic problem, thus allowing to describe the sinusoidal response to the sinusoidal load by solving one single static problem (as discussed in section 3.1). As adhesion occurs at the interface, the tangential stiffness K_t increases. An empirical quadratic dependency of K_t on the degree of adhesion D_a defined hereunder (section 3.2.3) is assumed:

$$K_t = \frac{E_{comp}}{h}\left(2 \times 10^{-3} + D_a^2\right) \cdot \tag{8}$$

When D_a reaches 1, full sticking occurs and K_t reaches the very high value of E_{comp}/h where $h = 2\,\mu$m is a very thin equivalent layer thickness ($\sim 1\%$ of the film's thickness).

Normal stress. After solving the elastic problem, one gets the horizontal displacement discontinuity $\delta u^*(x)$ across the interface, for each position x along the interface. Back to the temporal space, the discontinuity writes:

$$\delta u(x) = \delta u^*(x) \sin(\omega t) \tag{9}$$

and the velocity discontinuity

$$\delta v(x) = \delta u^*(x)\, \omega \cos(\omega t)\,. \tag{10}$$

The tangential stress τ, even though it was neglected while computing the elastic problem, can be approximated assuming a Coulombic friction. It then depends on the normal stress magnitude N applied on the interface. This normal force is the sum of an oscillating term σ_n linked to the vibration and a static term P_{app} linked to the sonotrode static holding force:

$$N = P_{app} + |\sigma_n|(t)\,. \tag{11}$$

For an order of magnitude approximation, P_{app} can be considered uniform on the whole interface thus leading to

$$P_{app} = \frac{F_{imp}}{A}, \tag{12}$$

where F_{imp} is the sonotrode holding force, of the order of 500 N, and $A = 323\,\text{mm}^2$ is the overlap area, such that

$$P_{app} \sim 1.5 \times 10^6\,\text{Pa}. \tag{13}$$

On the other hand, a lower bound of σ_n can be obtained by considering a uniform vertical sinusoidal deformation of amplitude a/h within the whole system thickness $h = h_{film} + 2h_{plates}$, $a \sim 80\,\mu$m being the sonotrode displacement amplitude. Using the PEI Young's modulus $E' \sim 4\,$GPa (see Appendix A) as a minimum bound for the system stiffness, the vertical stress $|\boldsymbol{\sigma}_n|$ is therefore bounded by:

$$|\boldsymbol{\sigma}_n| > E' \frac{a}{h_{film} + 2h_{plates}} \sim 8 \times 10^7\,\text{Pa}. \tag{14}$$

This shows that the vibrating term in equation (11) is significantly higher than the static term. The normal stress N on the interface can therefore be reduced to the term σ_n.

Using the Coulomb friction behaviour the tangent stress then writes:

$$\tau(x) = \mu.\,|\sigma_n(x)| \left(\frac{\delta v(x,y)}{|\delta v(x,y)|} \right). \tag{15}$$

where μ is the friction coefficient, that depends on temperature, and was obtained using a friction setup, at McGill University, as described in Appendix B. The parenthesis shows that the tangential force is always acting against slippage. σ_n is obtained from the elastic problem as:

$$\sigma_n(x) = \sigma^*_{yy}(x)\sin(\omega t) \tag{16}$$

$\sigma^*_{yy}(x) = \boldsymbol{\sigma}^*(x)\cdot\boldsymbol{e}_y\cdot\boldsymbol{e}_y$ being the vertical stress on the horizontal interface obtained by solving the normalized problem presented in section 3.1.

Dissipation. The average dissipated mechanical work associated to friction during an ultrasonic cycle writes

$$\dot{Q}_{fric}(x) = \langle \tau \cdot \delta v \rangle \tag{17}$$

the operator $\langle\cdot\rangle$ being the average operator over an ultrasonic vibration period $2\pi/\omega$. Noting that

$$\left(\frac{\delta v}{|\delta v|}\right)\cdot\delta v = |\delta v| \tag{18}$$

it gives

$$\dot{Q}_{fric}(x) = \alpha_h^2\frac{\omega}{2\pi}\times\int_0^{\frac{2\pi}{\omega}}\mu\left|\sigma^*_{yy}(x)\sin(\omega t)\right|\cdot\left|\delta u^*(x)\,\omega\cos(\omega t)\right|dt \tag{19}$$

where the hammering coefficient α_h accounts for the part of the cycle when contact is lost between the sonotrode and the sample. Developing leads to:

$$\dot{Q}_{fric}(x) = \alpha_h^2\frac{\omega^2}{2\pi}\mu\left|\sigma^*_{yy}(x)\,\delta u^*(x)\right|\times\int_0^{\frac{2\pi}{\omega}}\left|\sin(\omega t)\cos(\omega t)\right|dt \tag{20}$$

and finally

$$\dot{Q}_{fric}(x) = \alpha_h^2\frac{\omega}{\pi}\mu\left|\sigma^*_{yy}(x)\,\delta u^*(x)\right|. \tag{21}$$

Note that this friction dissipated power is proportional to the vibration frequency ω. This is related to the dry friction behavior assumed in eq. (15).

3.2.2. Intimate contact evolution

During the welding, the quality of the contact between the adherends and the flat energy director will evolve as the surface asperities get squeezed. During the last couple of decades, several models have been proposed to predict the evolution of this contact.

In the present study the Lee and Springer (1987) model is used to predict the intimate contact evolution. The degree of intimate contact D_{ic} is a scalar defined as the contact area ratio, and reaches 1 when full contact is obtained. The Lee and Springer model, followed by (Mantell and Springer, 1992) has been widely used in the literature (Ageorges et al., 2001), and proved its efficiency. The model for D_{ic} writes:

$$D_{ic}(x) = \frac{1}{w^*}\times\left[1 + a^*\int_0^t\frac{P_{app}}{\eta(T(x))}\right]^{\frac{1}{5}} \tag{22}$$

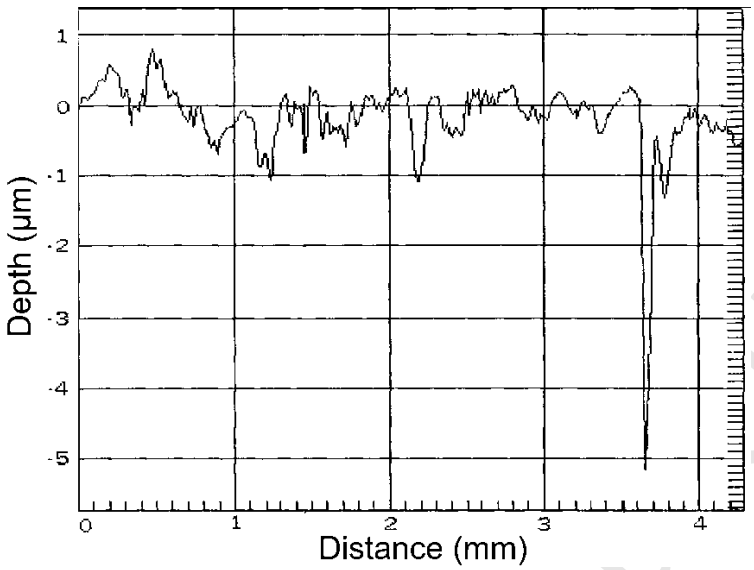

Figure 6: Contact surface profile of the composite.

Table 1: Intimate contact parameters.

$a_0[\mu\text{m}]$	$\frac{a_0}{b_0}$	$\frac{w_0}{b_0}$	w^*	a^*	$R_c = \frac{(a^*)^{\frac{1}{5}}}{w^*}$	$D_{ic0} = \frac{1}{w^*}$
0.2	1	0.7	1.7	8.5	0.9	0.588

where $w^* = 1 + w_0/b_0$ and $a^* = 5w^* (a_0/b_0)^2$ are geometric parameters related to the interface roughness. Using contact surface profile measurements presented in Fig. 6, Yang and Pitchumani (2001) proposed to directly obtain a_0 as the standard deviation of the surface function. This was also the approach followed by Levy et al. (2013). Nonetheless the other parameters b_0 and w_0 cannot be obtained. In this study the parameters used are simply adapted from the literature and are given in table 1. P_{app} is the static load applied on the interface, i.e. the sonotrode holding force divided by the overlap area, and $\eta(T(x))$ is the viscosity of the roughness, that is taken as the pure matrix viscosity (Levy et al., 2013). It follows an Arrhenius law

$$\eta(T) = A \times \exp\left(\frac{E_a}{RT\,[K]}\right) \tag{23}$$

where R is the gas constant. The pre-exponential factor A and the free energy E_a are determined experimentally using rheometry measurements (see Fig. 7).

$$\begin{aligned} A &= 7.23 \times 10^{-7}\,\text{Pa.s} \\ E_a &= 111.7\,\text{kJ/mol} \end{aligned} . \tag{24}$$

Equation (22) and (23) give the evolution of D_{ic} as an ordinary differential equation:

$$\frac{\partial D_{ic}}{\partial t} = D_{ic}^{-4} \left(\frac{a_0}{b_0}\right)^2 \times \left(\frac{1}{1+\frac{w_0}{b_0}}\right)^4 \frac{P_{app}}{A} \exp\left(-\frac{E_a}{T(x)}\right). \tag{25}$$

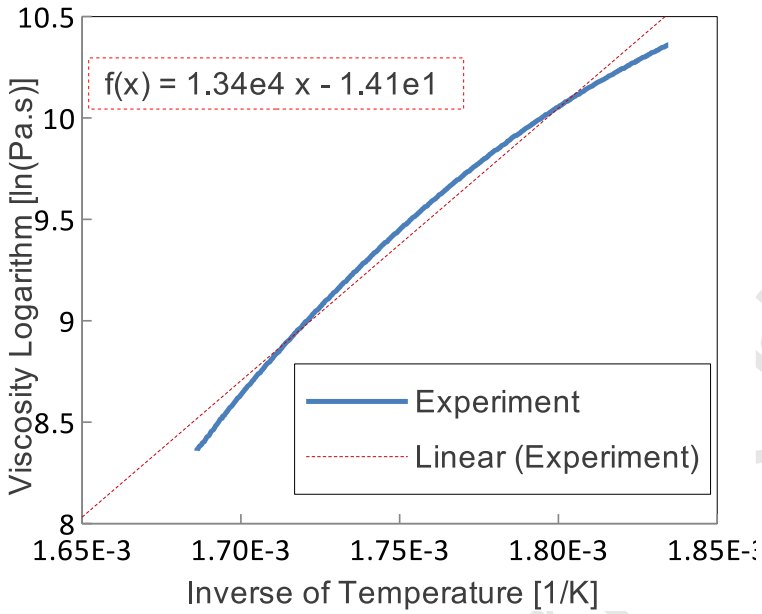

Figure 7: Logarithm of viscosity versus inverse of temperature for PEI resin. The linear fit gives the Arrhenius parameters.

The bad contact also results in a temperature gap at the interface. The thermal contact resistance associated with this gap decreases as the contact increases (as D_{ic} increases). In this study this resistance evolves according to the empirical relation proposed by Levy et al. (2013):

$$R_c\left(D_{ic}\left(x\right)\right) = D_{ic}\left(t=0\right) \times a_0 \left(\frac{1}{kD_{ic}^2\left(x\right)} + \frac{1-D_{ic}\left(x\right)}{k_{air}D_{ic}\left(x\right)} + \frac{1}{k}\right), \tag{26}$$

k being the thermal conductivity of the matrix and k_{air} of the air. $k_{air} = 0.03\,\mathrm{W/mK}$ shall be used.

Note that because the temperature is not continuous across the interface, the interfacial source $\dot{Q}_{fric}$ (eq. 21) is equally split on each side of the interface.

3.2.3. Adhesion evolution

In order to get a good adhesion, once intimate contact is achieved, the bond must be kept hot enough, and for a time long enough, to ensure diffusion of the polymer macromolecules across the interface. Following the reptation theory by De - Gennes (1971), the reptation time t_r represents the time the macromolecule needs to fully change its configuration. t_r can be modeled using an Arrhenius law:

$$t_r = A_r \exp\left(\frac{E_a}{R.T\,[K]}\right). \tag{27}$$

The complex viscoelastic moduli at high temperature were measured at $f = 10\,\mathrm{Hz}$ with a rheometer as shown in Fig. 8. Using the Cox-Merck principle (Ferry, 1980), the characteristic time

$$t_r = \frac{1}{2\pi f} = 15.9\,\mathrm{ms} \tag{28}$$

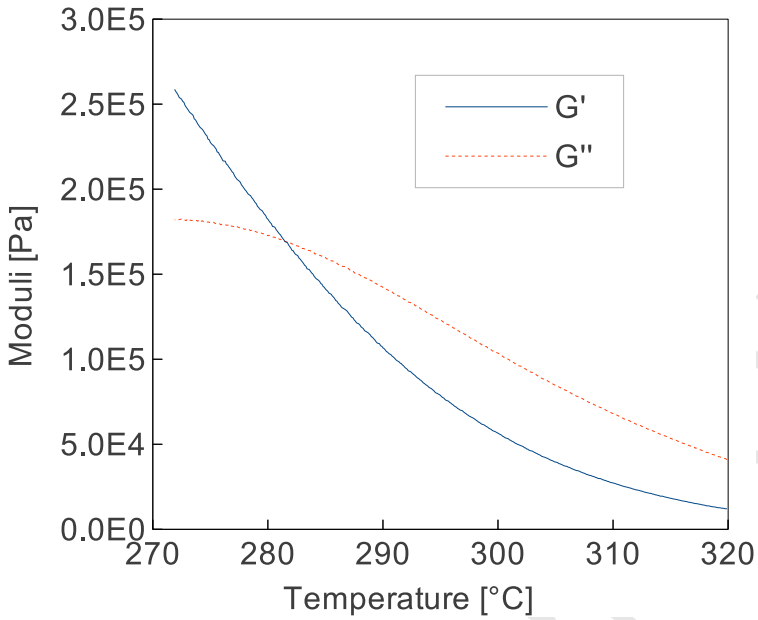

Figure 8: Elastic and Loss Moduli versus temperature for PEI measured at 10 Hz. The relaxation temperature of 281.5 °C is obtained.

is associated to this test. Following (Whorlow, 1992) this is the relaxation time at 281.5 °C where the two curves cross.which is the relaxation temperature for this test. Using eq. (27), A_r is identified at this temperature as:

$$A_r = 4.71 \times 10^{-13}\,\mathrm{s} \tag{29}$$

Once the macromolecule has fully diffused across the interface, healing is complete. Therefore, the degree of healing D_h is defined such that (Regnier et al., 2007):

$$\frac{\partial D_h}{\partial t} = \frac{1}{t_r\left(T\right)}. \tag{30}$$

Lee and Springer (1987) proposed a coupled model to ensure that only the surface already in intimate contact starts healing. Butler et al. (1998) extended the idea and investigated which of the intimate contact or healing is the limiting phenomenon. Yang and Pitchumani (2003) suggested an improvement of the intimate contact model but kept the coupled model idea. Based on these models, the degree of adhesion

$$D_a = D_{ic} \times D_h \tag{31}$$

is defined. It ensures that only the fraction in intimate contact heals. $D_a\left(x\right)$ is computed for each position x of the interface using D_{ic} and D_h obtained by solving the ordinary differential equations (25) and (30).

3.3. Implementation

The model is solved with finite element methods using the commercial software COMSOL multiphysics. Thanks to the symmetries of the system, a quarter of the two dimensional geometry is simulated (see Fig. 9).

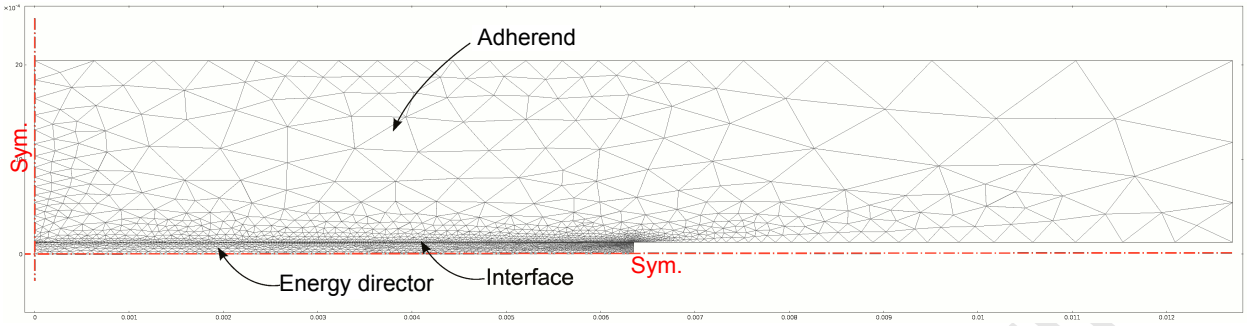

Figure 9: Mesh over the computation domain.

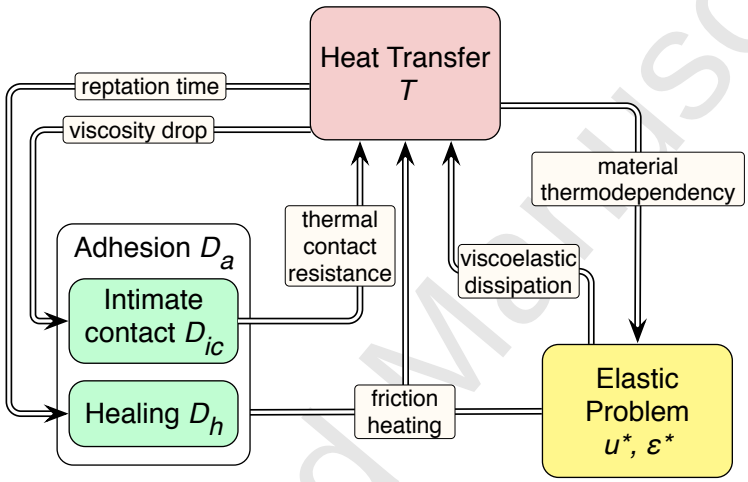

Figure 10: The three physical problems to be solved and their couplings.

It consists of half the upper composite adherents and a quarter of the flat energy director. The quarter geometry is meshed with 5063 unstructured triangles with refinement along the interface. The unknowns are: (i) the displacement vector and (ii) the temperature in the whole domain, obtained by solving the elastic problem and the heat transfer using a quadratic interpolation; and (iii) the degree of intimate contact and (iv) the degree of healing at each node of the interface. The couplings are summarized in Fig. 10.

A backward Euler solver is used for the time integration. The resolution is stopped when the minimum temperature in the film exceeds $T_g + 20\,^{\circ}\mathrm{C}$, $T_g = 215\,^{\circ}\mathrm{C}$ being the glass transition temperature of the PEI. This temperature is reached before 0.5 s. The computation is performed on a desktop computer in less than 5 min.

Following the experimental procedure, at initial time $t = 0$, the sonotrode holding force F_{imp} is applied. Then, the amplitude $a\,(t)$ of the displacement imposed by the sonotrode on the upper part of the assembly starts increasing. It is ramped from 0 at $t = 0$ to the nominal amplitude at time $t = t_{ramp}$. The reference case presented in Fernandez Villegas (2013) is replicated. The parameters that were not given in the text are in table 2.

Table 2: Parameters used in the reference simulation.

α_h	hammering coefficient	0.32
ω	sonotrode pulsation	125000 rad.s^{-1}
a	sonotrode amplitude	86.2 μm
t_{ramp}	time to establish vibration	50 ms
P_{app}	sonotrode holding pressure	1.55 MPa

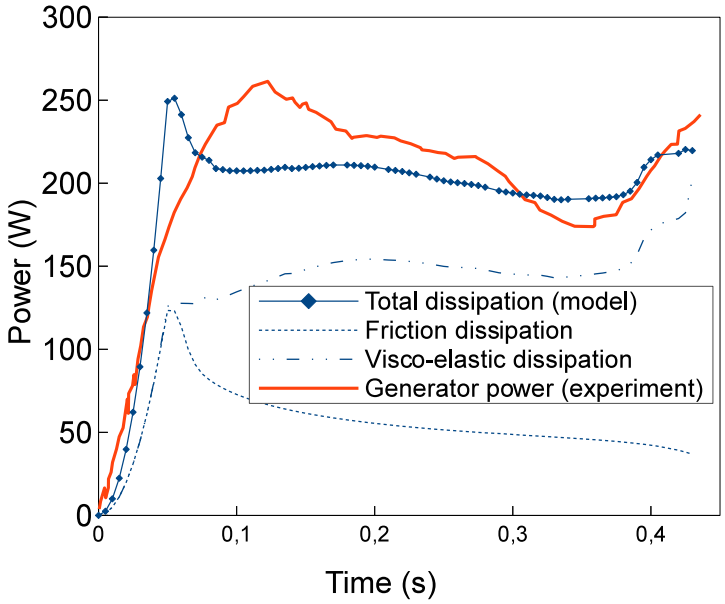

Figure 11: Total simulated dissipated powers and measured transmitted power Fernandez Villegas (2013) (assuming an efficiency $\chi = 13\%$) versus time. Reference case with a sonotrode amplitude of 86.2 μm and a holding force of 500 N.

4. Results and Discussion

4.1. Dissipated powers

Fig. 11 shows the different powers dissipated in the system. It was obtained by integrating successively the visco-elastic dissipation $\dot{Q}_{bulk}$ (eq. (6)), the friction dissipation $\dot{Q}_{fric}$ (eq. (21)) and the sum of both (the *total dissipation*) over the domain.

Fernandez Villegas (2013) measured the experimental electric power delivered to the ultrasonic apparatus P_{rig}. Because of several losses, amongst which:

- the generator efficiency itself
- acoustic losses
- dissipation in the composite plates
- dissipation/damping in the rig

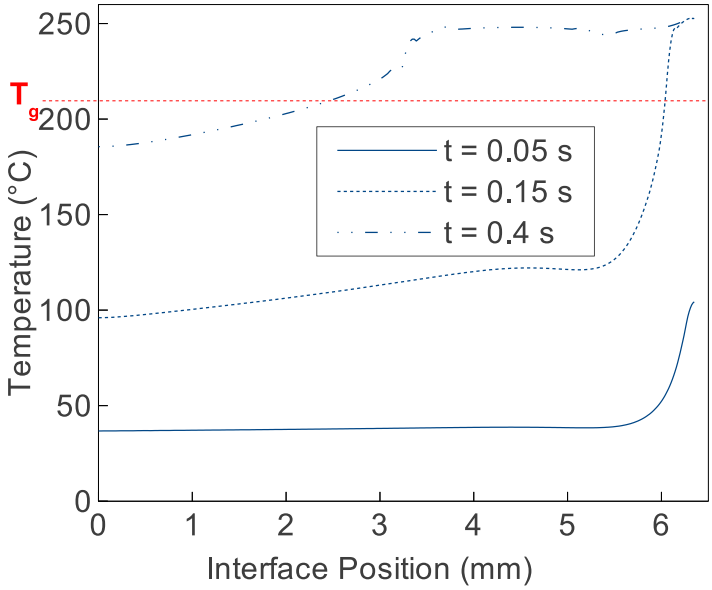

Figure 12: Temperature predictions along the interface at three characteristic times.

only a fraction of this delivered power was dissipated in the system. Considering a constant efficiency $\chi = 13\%$, the experimental dissipated power $P_{exp} = \chi \cdot P_{rig}$ fitted with the predicted total dissipation.

In Fig. 11 after the initial ramp that corresponds to the sonotrode amplitude increase, a first peak around $t_{ramp} = 0.05\,\mathrm{s}$ is associated with the highest friction dissipation. Despite the good qualitative representativity of the obtained power curves, there is a systematic discrepancy in this initial stage, which is also visible for other processing conditions (see Figs. 17 and 18). This effect is mainly due to the modeling of the sonotrode transient regime. In practice, just after the contact with the plates, the vibration amplitude starts from zero to the desired value within a certain duration. Only after this stage, a stationary regime of the loading is reached. In order to simulate this initial step, a linear variation of the vibration amplitude a was imposed, which led to a somewhat quadratic evolution of the dissipated energy, as it can be expected from Eqs. (7) and (21).

Following that peak, adhesion started, such that the friction dissipation quickly decreased, leading to a slight decrease of the total power. Around $t_{min} = 0.38\,\mathrm{s}$, accurately reproducing the experimental trend, the power rose.

4.2. Temperature predictions

Fig. 12 presents the temperature along the center of the energy director film at three different characteristic times. Note that because of symmetry only a half of the interface is plotted and position 0 corresponds to the center of the film. At $t_{ramp} = 0.05\,\mathrm{s}$, the temperature showed a slight increase at the edge of the energy directors. This is explained by the slippage at the interface that is higher at the edge than at the

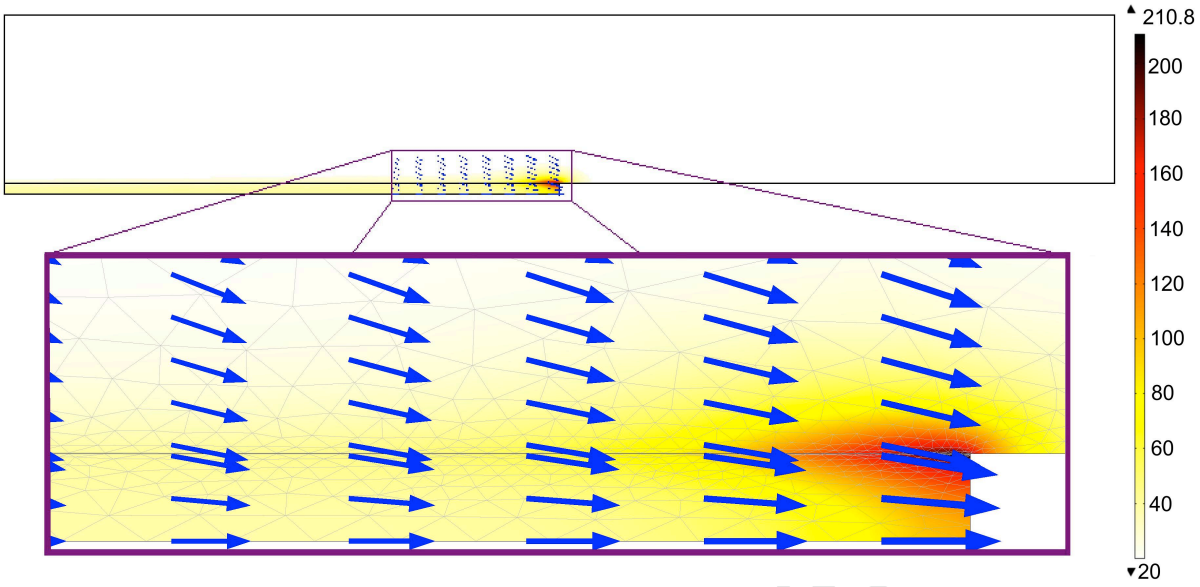

Figure 13: Temperature and displacement fields at time $t_{ramp} = 0.05\,\mathrm{s}$. General view and closeup.

center (as shown in Fig. 13). It induces a higher friction dissipation. Then, the temperature increased until $t = 0.15\,\mathrm{s}$, when the hottest point (the edge) reached the PEI glass transition temperature $T_g = 215\,^{\circ}\mathrm{C}$. Then, the visco-elastic dissipated power was steady (as shown in Fig. 11), as a larger part of the film reached the glass transition temperature. Eventually, at time $t = 0.4\,\mathrm{s}$, the whole film almost reached the glass transition temperature. The system stiffness dropped and allowed for higher deformation amplitudes in the film. In addition with the increased loss modulus of the polymer around T_g, the total visco-elastic dissipation quickly increased. This was observed experimentally by Fernandez Villegas (2013) and corresponds to the beginning of the flow.

Fig. 14 presents the temperature profile across the adherends and the flat energy director at three different locations: in the middle of the sample, at three quarters and at the edge of the film. Once again, for symmetry reasons, only a quarter of the domain is considered. The temperatures are plotted at time $t = 0.4\,\mathrm{s}$. During this initial heating phase, the heating of the bond was very local. That is very encouraging for an efficient welding without deconsolidation of the adherends. This was, once again, experimentally observed Fernandez Villegas (2013), during this initial heating phase. One should finally notice that the temperature in the middle plane of the film ($y = 0$) is higher than the temperature at the interfaces energy director/adherends ($y = 0.125\,\mathrm{mm}$), which shows that flow might start in the flat energy director centerplane before the interfaces reach T_g.

4.3. Adhesion evolution

Fig. 15 shows the degree of adhesion along the energy director/adherends interface at different times. At time $t = 0.1\,\mathrm{s}$, because of the higher temperatures, adhesion started at the edge (around $x = 6\,\mathrm{mm}$).

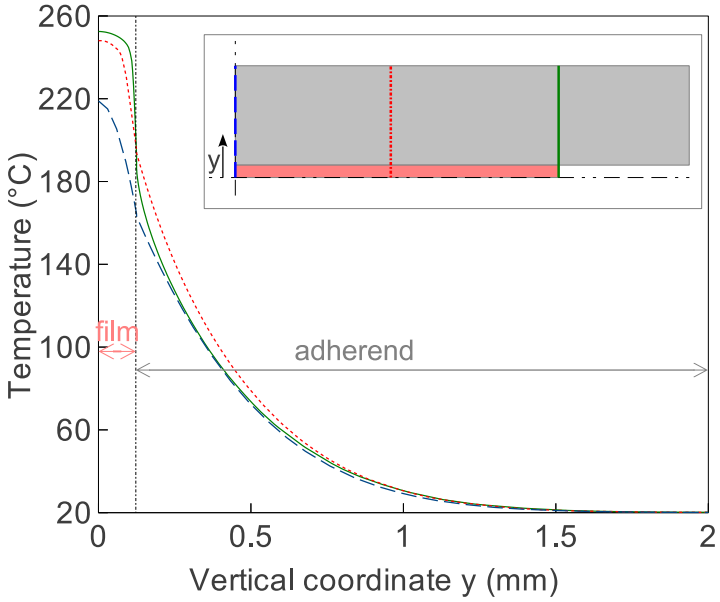

Figure 14: Predicted temperature profile at $t = 0.4\,\mathrm{s}$ across the assembly thickness at three locations: bond centerline (- -), bond quarter (··) and bond edge (–). Heating is localized in the energy director.

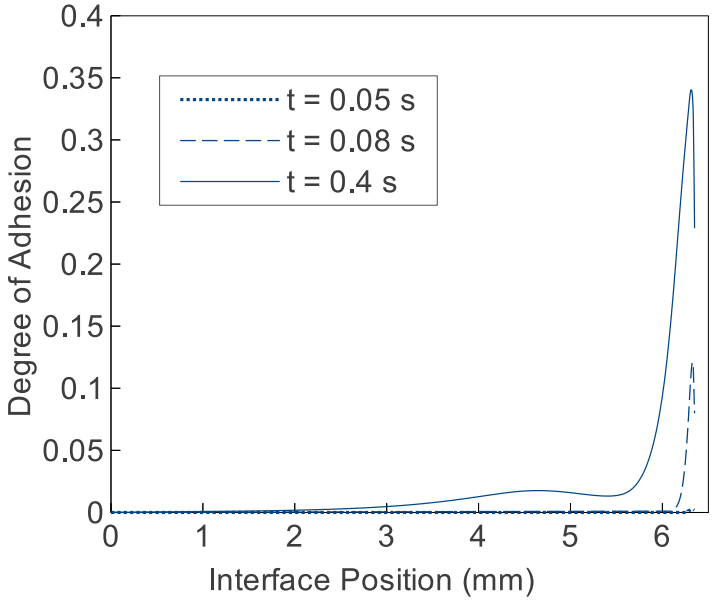

Figure 15: Predicted degree of adhesion at different times along the interface. Adhesion starts at 0.05 s at the edge of the overlap.

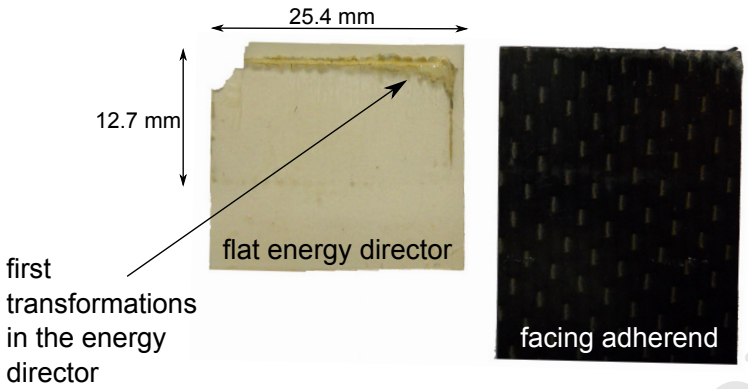

Figure 16: First physical transformations occur at the edges of the energy director and leave no significant traces on the composite adherends (100 ms vibration time at 500 N and 86.2 μm) (Fernandez Villegas, 2013).

This was confirmed experimentally by Fernandez Villegas (2013). As shown in Fig. 16, weak adhesion starts at the edges. Right after that, heating and adhesion increased everywhere in the interface. At time $t = 0.4$ s, the degree of adhesion was non negligible everywhere along the interface, which was also observed experimentally.

4.4. Parametric study

A second simulation was performed with a higher sonotrode holding force $F_{imp} = 1500$ N to reproduce the case 1500 N/86.2 μm investigated by Fernandez Villegas (2013). Because a higher holding force results in a reduced hammering effect, the hammering coefficient was increased to $\alpha_h = 0.38$. Using the same efficiency $\chi = 13\%$, the simulated power curve accurately predicts the plateau, followed by the increase around 0.22 s, as shown in Fig. 17.

Note that the the friction dissipation $\dot{Q}_{fric}$ (eq. (21)) does not depend directly on the sonotrode holding force because the effect of P_{app} was assumed to be negligible. A higher holding force will only result in a decreased hammering effect and thus, a higher energy transfer, and faster heating (term α_h in eq. (21)). Indeed, the tangential vibrating interfacial force τ (eq. 15) is significantly higher than the static tangential force μP_{app} acting at the interface as discussed in section 3.2.1.

The higher holding force also resulted in a faster intimate contact and thus a faster adhesion. In that case, where $F_{imp} = 1500$ N, the maximum degree of adhesion at the end of the heating phase (at $t = 0.25$ s) reached 0.34. As visible in figure 15, it is comparable to the maximum obtained in the reference case, where $F_{imp} = 500$ N, after a shorter heating phase ($t = 0.4$ s).

A third simulation was performed with a lower holding force $F_{imp} = 300$ N and a smaller sonotrode amplitude $a = 51.8\,\mu$m. The lower sonotrode amplitude led to a reduced hammering effect even though the holding force was reduced. Indeed, using a hammering coefficient $\alpha_h = 0.39$ led to an acceptable recovery of the dissipated power, as shown in Fig. 18.

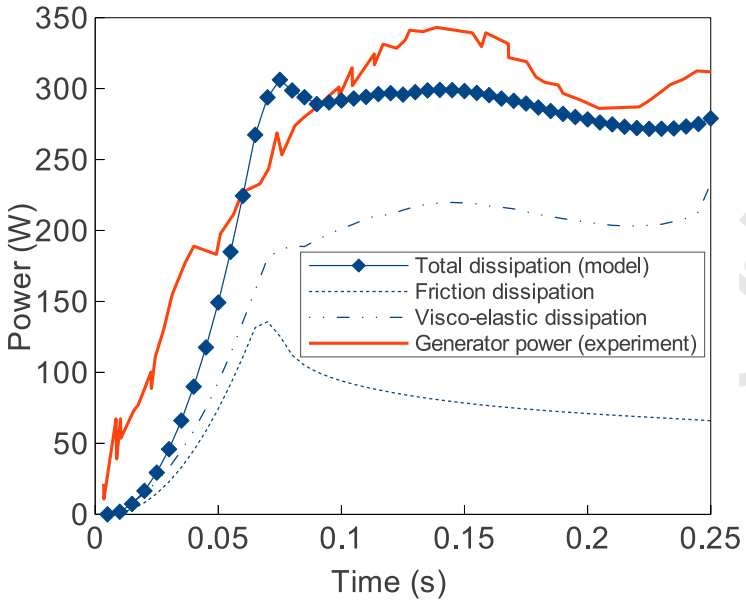

Figure 17: Total simulated dissipated powers and measured transmitted power Fernandez Villegas (2013) (assuming an efficiency $\chi = 13\%$) versus time. Sonotrode amplitude of 86.2 μm and holding force of 1500 N.

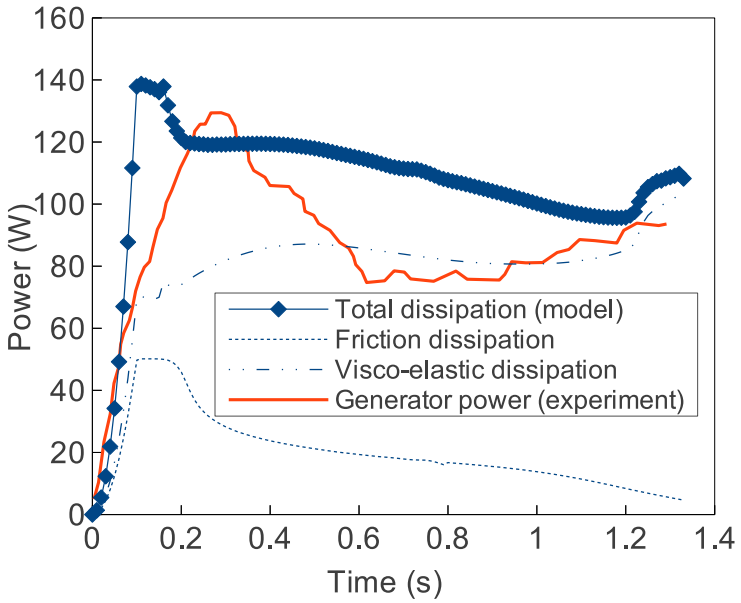

Figure 18: Total simulated dissipated powers and measured transmitted power Fernandez Villegas (2013) (assuming an efficiency $\chi = 13\%$) versus time. Sonotrode amplitude of 51.8 μm and holding force of 300 N.

The developed numerical tool consistently approximated the experimental measurements, for different holding forces and sonotrode amplitudes. The only parameter to fit was the hammering coefficient, which was shown to control the transmitted power in the process and the magnitude of the total dissipation. In the presented simulations, α_h was set to a constant empirical value, but more efforts are necessary to better model the evolution of this parameter with the sonotrode amplitude and holding force.

5. Conclusions

Ultrasonic welding of Carbon/PEI composite was investigated. A neat PEI film at the interface between the two plates to be welded acts as a flat energy director. It allows a local heating and ensures a progressive adhesion of the two adherends to be welded. The main contributions of the present work are the following:

- A numerical multiphysical model of the leading physical phenomena occurring during the heating phase was developed. The model consists of:
  - an elastic problem that predicts the effects of the ultrasonic vibration
  - a heat transfer problem, that predict the temperature increase
  - and a coupled bonding evolution problem at the interface, that predicts the evolution of the adhesion.
- The simulations aimed at replicating the experiments given in Fernandez Villegas (2013).
  - The results confirm that the heating is mostly initiated by friction dissipation between the flat energy director and the composite adherends.
  - Once adhesion occurs, slippage is reduced and friction drops while viscoelastic dissipation takes over.
  - The temperature at the interface progressively increases until it reaches the glass transition temperature. Afterwards, the flow of the resin can start, and the heating phase is finished.
- The predicted dissipated powers were compared with the experimental electric power delivered to the ultrasonic unit. A transmitted power of 13% of the apparatus power was found to accurately fit the predicted dissipated power in the bond for three different combinations of welding parameters.

Acknowledgement

The authors would like to thank professor Pascal Hubert without whom this collaboration would not have been possible. The authors also acknowledge the help of Marcus Scaramanga with the design and manufacturing of the friction measurement apparatus.

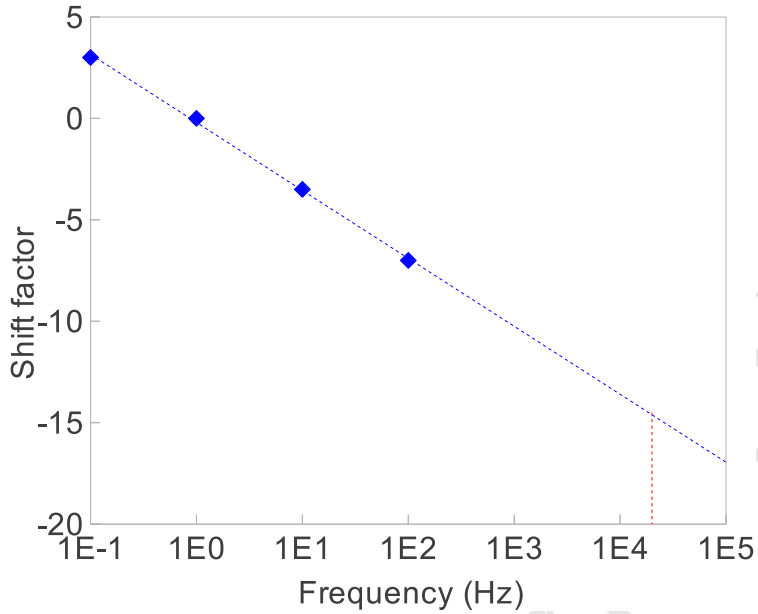

Figure A.19: Obtained shift factor and its extrapolation to 20 kHz.

Appendix A. Determination of the viscoelastic modulus at high frequency

The elastic and loss moduli E' and E'' of the neat PEI were measured using a DMA apparatus between room temperature and 235 °C for five frequencies f: 0.1, 1, 10 and 100 Hz. Using a time temperature superposition principle, the obtained data were shifted onto the $f = 1$ Hz master curve, assuming that:

$$E'(T, f) = E'(T + a(f \to 1), 1) \tag{A.1}$$

and

$$E''(T, f) = E''(T + a(f \to 1), 1). \tag{A.2}$$

The obtained shift factors $a(f \to 1)$ are plotted for each frequency in Fig. A.19. Extrapolation of this shift factor to 20 kHz gives:

$$a(20\,\text{kHz} \to 1\,\text{Hz}) = -14.5\,^{\circ}\text{C}. \tag{A.3}$$

The elastic and loss moduli of PEI at 20 kHz, obtained using this shift factor, and used in this study, are shown in Fig. A.20.

Appendix B. Measurement of the friction coefficient

The classical coulomb law has been widely used to characterize composite friction behavior. It consists in considering a behavior such that a constant friction coefficient μ can be determined as:

$$\mu = \frac{T}{N} \tag{B.1}$$

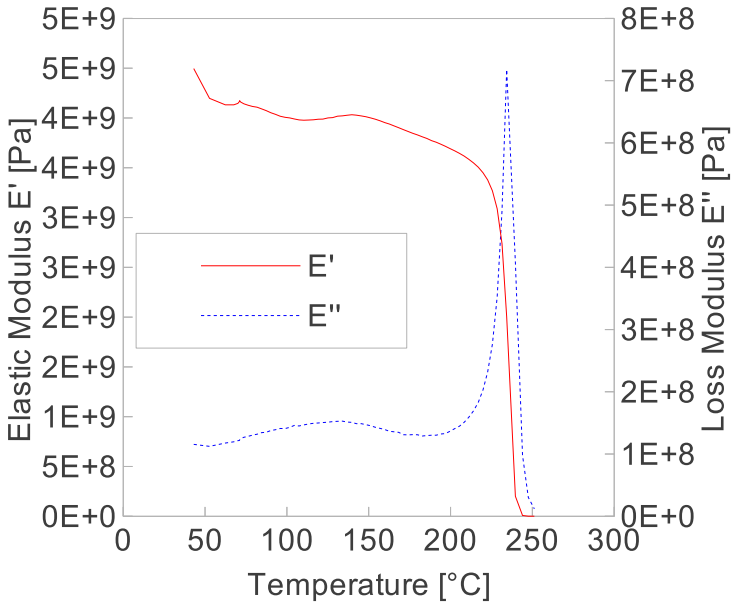

Figure A.20: Elastic and loss moduli of PEI at 20 kHz.

Table B.3: Friction coefficient measurements.

Velocity mm/s	Normal Force kPa	Friction coefficient μ
1.17	86	0.189
2.33	86	0.196
1.17	129	0.201
2.33	129	0.196
		$0.195 \pm 3\%$

where T is the tangent load and N is the normal load applied between the adherend and the energy director.

μ was determined using a friction setup based on the ASTM method D1894 (ASTM International, 1995), initially developed for measuring thin plastic sheet friction coefficient. The setup was similar to the one proposed by Thije and Akkerman (2009), Lebrun et al. (2004) or Sun et al. (2013). It consisted of two platens that applied a controlled normal load and was installed in an MTS tensile machine (depicted in Fig. B.21). Two PEI films similar to those used as flat energy directors were attached on each platen, and a CF/PEI plate, similar to the adherends used in the study, was compressed between those wrapped platens. The contact area was that of the platens: 50.8 mm × 101.6 mm. Normal loads corresponding respectively to 86 and 129 kPa were applied and the plate was pulled through, using the MTS machine, at a constant velocity of successively 1.17 $^{mm}/_{s}$ and 2.33 $^{mm}/_{s}$. The measured extraction force was averaged over steady state phase of the test, that was reached after about 20 mm . Using the two normal loads, values of the friction coefficient were obtained. The test was performed at room temperature. Results are given in table B.3.

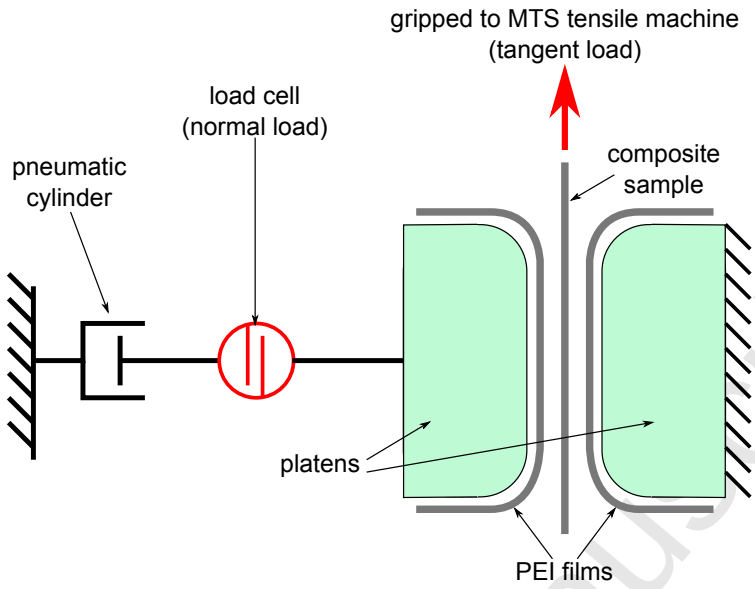

Figure B.21: Friction coefficient measurement setup comprising two platens and the tensile machine grip for tangent load.

The four friction coefficient obtained using the two different normal and two different velocities presented less than 10% dispersion and showed the adequacy of the Coulomb law. An average of these four values was used in the simulation. Note that only the room temperature behavior was studied since the friction will mostly occur at the initial stage of the process, at low temperature.

References

Ageorges, C., Ye, L., Hou, M., 2001. Avdances in Fusion Bonding Techniques for Joining Thermoplastic Matrix Composites: a Review. Composites Part A: applied science and manufacturing 32, 839–857.

ASTM International, 1995. ASTM D1894 - 93. Standard Test Method for Static and Kinetic Coefficients of Friction of Plastic Film and Sheeting.

ASTM International, 2010. ASTM D1002 - 10 Standard Test Method for Apparent Shear Strength of Single-Lap-Joint Adhesively Bonded Metal Specimens by Tension Loading (Metal-to-Metal).

Augh, L., Gillespie Jr, J.W., Fink, B., 2001. Degradation of continuous carbon fiber reinforced polyetherimide composites during induction heating. Journal of Thermoplastic Composite Materials 14, 96–114.

Benatar, A., Eswaran, R.V., Nayar, S.K., 1989. Ultrasonic welding of thermoplastics in the near-field. Polymer Engineering and Science 29, 1689–1698.

Benatar, A., Gutowski, T.G., 1989. Ultrasonic Welding of PEEK Graphite APC-2 Composites. Polymer Engineering and Science 29, 1705–1721.

Butler, C.A., Mccullough, R.L., Pitchumani, R., Gillespie Jr, J.W., 1998. An analysis of mechanisms governing fusion bonding of thermoplastic composites. Journal of Thermoplastic Composite Materials 11, 338.

De - Gennes, P.G., 1971. Reptation of a polymer chain in the presence of fixed obstacles. The Journal of Chemical Physics 55, 572.

Fernandez Villegas, I., 2013. In Situ Monitoring of Ultrasonic Welding of Thermoplastic Composites Through Power and Displacement Data. Journal of Thermoplastic Composite in press.

Ferry, J.D., 1980. Viscolelastic Properties of Polymers. John Wiley and Sons.

Grewell, D., Benatar, A., 2007. Welding of plastics: Fundamentals and new developments. International Polymer Processing 22, 43–60.

Jacquet, E., Trivaudey, F., Varchon, D., 2000. Calculation of the transverse modulus of a unidirectional composite material and of the modulus of an aggregate. Application of the rule of mixtures. Composites Science and Technology 60, 345–350.

Lebrun, G., Bureau, M.N., Denault, J., 2004. Thermoforming-Stamping of Continuous Glass Fiber/Polypropylene Composites: Interlaminar and Tool-Laminate Shear Properties. Journal of Thermoplastic Composite Materials 17, 137–165.

Lee, W.I., Springer, G.S., 1987. A model of the manufacturing process of thermoplastic matrix composites. Journal of Composite Materials 21, 1017–1055.

Levy, A., Heider, D., Tierney, J., Gillespie, J., 2013. Inter-layer Thermal Contact Resistance Evolution with the Degree of Intimate Contact in the Processing of Thermoplastic Composite Laminates. Journal for Composite Materials .

Levy, A., Le Corre, S., Chevaugeon, N., Poitou, A., 2011a. A levelset based approach for the finite element simulation of a forming process involving multiphysics coupling : ultrasonic welding of thermoplastic composites. European Journal of Mechanics - A/Solids 30, 501–509.

Levy, A., Le Corre, S., Poitou, A., 2012. Ultrasonic welding of thermoplastic composites: a numerical analysis at the mesoscopic scale relating processing parameters, flow of polymer, and quality of adhesion. International Journal of Material Forming in press.

Levy, A., Le Corre, S., Poitou, A., Soccard, E., 2011b. Ultrasonic Welding of Thermoplastic Composites, Modeling of the Process Using Time Homogenization. International Journal for Multiscale Computational Engineering 9, 53–72.

Mantell, S., Springer, G., 1992. Manufacturing process models for thermoplastic composites. Journal of Composite Materials 26, 2348–2377.

Nonhof, C.J., Luiten, G.A., 1996. Estimates for Process Conditions During the Ultrasonic Welding of Thermoplastics. Polymer Engineering and Science 36, 1177–1183.

Regnier, G., Nicodeau, C., Verdu, J., Cinquin, J., Chinesta, F., 2007. A Multi-physic and Multi-scale Approach to Model the Continuous Welding of Thermoplastic Matrix Composites, in: ICCM 16, Kyoto, Japan. pp. 1–6.

Sun, J., Li, M., Gu, Y., Zhang, D., Li, Y., Zhang, Z., 2013. Interply friction of carbon fiber/epoxy prepreg stacks under different processing conditions. Journal of Composite Materials in press.

Suresh, K.S., Roopa Rani, M., Prakasan, K., Rudramoorthy, R., 2007. Modeling of temperature distribution in ultrasonic welding of thermoplastics for various joint designs. Journal of Materials Processing Technology 186, 138–146.

Tencate Advanced Composites, 2008. Technical Data sheet. Cetex PEI.

Thije, R.H.W., Akkerman, R., 2009. Design of an experimental setup to measure tool-ply and ply-ply friction in thermoplastic laminates. International Journal of Material Forming 2, 197–200.

Tolunay, M.N., Dawson, P.R., Wang, K.K., 1983. Heating and bonding mechanisms in ultrasonic welding of thermoplastics. Polymer Engineering and Science 23, 726–733.

Wang, X., Yan, J., Li, R., Yang, S., 2006. FEM Investigation of the Temperature Field of Energy Director During Ultrasonic Welding of PEEK Composites. Journal of Thermoplastic Composite Materials 19, 593–607.

Whorlow, R., 1992. Reological Techniques. Ellis horw ed., Series in Physics and its Applications, Chichester, England.

Yang, F., Pitchumani, R., 2001. A fractal Cantor set based description of interlaminar contact evolution during thermoplastic composites processing. Journal of Materials Science 36, 4661–4671.

Yang, F., Pitchumani, R., 2003. Nonisothermal healing and interlaminar bond strength evolution during thermoplastic matrix composites processing. Polymer Composites 24, 263–278.

Yousefpour, A., Hojjati, M., Immarigeon, J.P., 2004. Fusion Bonding/Welding of Thermoplastic Composites. Journal of Thermoplastic Composite Materials 17, 303–341.

Zhang, Z., Wang, X., Luo, Y., Wang, L., 2009. Study on Heating Process of Ultrasonic Welding for Thermoplastics. Journal of Thermoplastic Composite Materials 25, 647–654.

List of Figures